Research Article | Vol. 28, No. 25 / 7 December 2020 / Optics Express 37373

Optics EXPRESS

# *In situ* measurements of the volume scattering function with LISST-VSF and LISST-200X in extreme environments: evaluation of instrument calibration and validity

HÅKON SANDVEN, ARNE S. KRISTOFFERSEN, YI-CHUN CHEN, AND BØRGE HAMRE*

*Department of Physics and Technology, University of Bergen, Allegaten 55, 5007 Bergen, Norway*
**borge.hamre@uib.no*

**Abstract:** The LISST-VSF and LISST-200X are commercial instruments made available in recent years, enabling underwater measurements of the volume scattering function, which has not been routinely measured *in situ* due to lack of instrumentation and difficulty of measurement. Bench-top and *in situ* measurements have enabled absolute calibration of the instruments and evaluation of instrument validity ranges, even at environmental extremes such as the clear waters at the North Pole and turbid glacial meltwaters. Key considerations for instrument validity ranges are ring detector noise levels and multiple scattering. In addition, Schlieren effects can be significant in stratified waters.



## 1. Introduction

Changes in the ocean ecosystems due to anthropogenic climate change necessitates an increased level of environmental monitoring of the ocean. While ocean color data from remote sensing provide observations with extensive temporal and spatial coverage, it is often difficult to acquire accurate quantitative measurements of ocean constituents such as phytoplankton and colored dissolved organic matter (CDOM) in productive coastal regions [1,2]. Improvements in the ocean color products require enhanced measurements of the inherent optical properties (IOPs). These properties describe the influence of the water medium on light propagation, and are independent of the light field. These are measured *in situ*, typically with an active source and detector. Such optical *in situ* measurements can obtain high-resolution information about the vertical structure of the water column, which are unretrievable from satellite observations. While the spectral absorption and attenuation coefficients have been routinely measured for several years, direct measurements of scattering properties are more sparse. Unlike absorption, scattering also has a directional variability, quantitatively described by the volume scattering function (VSF). Due to lack of measurements, the VSF is often represented by simplified parameterisations, and scattering errors are corrected by empirical formulas. Thus, high-accuracy routine VSF measurements, which can be provided by the instruments LISST-VSF and LISST-200X, would be an important development within ocean optics research. This includes input for radiative transfer models, calculations of suspended particle properties [3,4], and corrections on other IOP measurements [5].

The volume scattering function (VSF or $\beta$, used interchangeably) is a fundamental IOP that represents the ability of a medium to scatter light in a certain direction. It is mathematically formulated as

$$\beta(\theta) = \frac{\mathrm{d}I(\theta)}{E\,\mathrm{d}V}\ [\mathrm{m}^{-1}\mathrm{sr}^{-1}], \tag{1}$$

#411177 https://doi.org/10.1364/OE.411177
Journal © 2020 Received 30 Sep 2020; revised 12 Nov 2020; accepted 12 Nov 2020; published 24 Nov 2020

Optics EXPRESS

where $E$ is the irradiance of an incident unpolarized beam, $\mathrm{d}I$ is the radiant intensity of the scattered light from the volume element $\mathrm{d}V$ at an angle $\theta$ relative to the incident beam. Here, no azimuthal dependency is assumed, which is the case for media with randomly oriented scatterers. The more routinely measured scattering coefficient $b$ can be calculated from the VSF using

$$b = 2\pi \int_0^\pi \beta(\theta) \sin\theta \mathrm{d}\theta. \tag{2}$$

Moreover, the phase function $p(\theta)$, which is the normalized VSF, is defined by $p(\theta) = \beta(\theta)/b$. While the scattering coefficient may vary with several orders of magnitude depending on the ocean constituents in the respective water mass, and wavelength to a lesser degree, the phase function tends to depend less on ocean constituents and wavelength in natural waters. Hence, the phase function has often been subject to simplified models in radiative transfer modelling. Other related quantities are the backscattering coefficient $b_b$, given by

$$b_b = 2\pi \int_{\pi/2}^\pi \beta(\theta) \sin\theta \mathrm{d}\theta, \tag{3}$$

and the asymmetry factor $g$,

$$g = \langle \cos\theta \rangle = \frac{2\pi}{b} \int_0^\pi \beta(\theta) \cos\theta \sin\theta \mathrm{d}\theta. \tag{4}$$

Due to the $\cos\theta$-term, the asymmetry factor is more dependent on scattering in the far-forward and far-backward direction than the scattering and backscattering coefficients, which makes it challenging to measure accurately. It is often applied when assessing whether multiple scattering can be neglected or not.

The VSF of a medium containing randomly distributed spheres of uniform size and homogeneous structure was fully solved by Gustav Mie as a solution of Maxwell's equations [6]. For monodispersed spheres, only particle concentration, the size parameter (particle diameter relative to wavelength), and the relative complex refractive index decide the VSF. The solution becomes much more complex for non-spherical particles (see work of Mishchenko, e.g. [7]), and non-homogeneous optical properties. This makes forward modelling of the VSF in natural waters challenging, and the inverse problem even more so. Among others, the Fournier-Forand model [8] and Zhang et al. [9] utilize assumptions about particle size distributions and compositions to approximate the VSF.

While the refractive index influences scattering at all angles, the VSF depends strongly on the particle size distribution in the forward direction. Hence, the particle size distribution can be measured from small-angle scattering measurements using inversion methods. Known as laser diffraction, this technique forms the physical motivation behind a series of LISST-instruments (Laser *In Situ* Scattering and Transmissometry, produced by Sequoia Sci.), which are routinely used for sediment and oceanographic studies. The working principle is illustrated in Fig. 1. A laser beam of known power is transmitted through a sample chamber. The transmitted light is detected by a transmission detector, from which the attenuation coefficient can be calculated. The scattered light passes through a lens and onto a ring detector placed at the lens' focal length. Hence, all light scattered with a certain angle from the beam hits the same radius on the ring, and is detected by the silicon photodetector arcs covering logarithmically-spaced radii and consequently scattering angles. Agrawal [10] demonstrated how the scattering data from the LISST-100 ring detector could be used to compute the shape of the VSF, with the angular resolution covered by the ring detector arcs. Slade and Boss [11] used polystyrene beads to calibrate LISST-100 scattering data, yielding both the correct VSF shape and magnitude for angles 0.08-15°. Later, multiple studies have utilized LISST instruments for VSF measurements [12–15]. In [16–18],

Optics EXPRESS

the Schlieren effect on forward scattering and attenuation have been investigated. However, the LISST-200X, which is the most recent successor of LISST-100 and measures the VSF for angles 0.04-13° at 670 nm, has not previously been calibrated or used for VSF measurements to our knowledge.

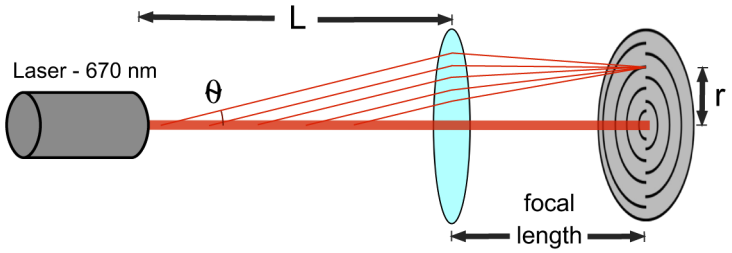


**Fig. 1.** The working principle of the ring detector used for LISST-200X. The detector plane is placed in the focal plane of a collimating lens, so that light scattered with angle $\theta$ will hit the detector plane at radius $r$. The LISST-VSF ring detector is similar, but with a 515 nm laser wavelength and a longer pathlength $L$.

The LISST-VSF is a recently released instrument measuring the VSF from 0.09° to 150°. Compared to the scattering and backscatter coefficients, as well as small-angle scattering, the large-angle VSF have been sparingly measured *in situ*. The primary reason is the technical difficulty of the measurements; due to the ratio of forward to backward scattered radiance there is a high demand on the dynamical range of the instrument. Tyler [19] and Petzold [20] were among the first attempts to measure the VSF, and the latter has emerged as the most widely cited set of VSF measurements. While the Petzold measurements are limited in geographical and environmental scope, they are of remarkable quality over a large angular range and are highly beneficial as benchmark figures. Modern studies have focused more on laboratory studies, but also includes some *in situ* measurements (see [21] for an overview). For the LISST-VSF, the dynamical range is covered by using the aforementioned ring detector up to 14.38°, and using a rotating eyeball detector at larger angles. The laser power is decreased when the eyeball position is between 15° and 40° to accommodate for the large differences in the scattering signal. In addition to the VSF, the eyeball detector also yields data allowing computation of Mueller matrix components $M_{12}$ and $M_{22}$.

There is still a limited number of published studies with *in situ* or bench-top results from the LISST-VSF. Slade et al. [22] contains the first published results with the LISST-VSF, with bench-top measurements of polystyrene and size-fractioned Arizona Test Dust. Here, the degree of polarization was measured in addition to the VSF. The instrument has been shown to agree well with two other prototype VSF instruments, I-VSF and POLVSM [23]. However, due to unfortunate instrument damage, only the ring detector measurements were usable in this study. In the article by Koestner et al. [24], measurements with polystyrene beads of diameters in the sub-micrometer range were used to show that a correction function, $\beta_p^{\mathrm{corr}}(\theta) = \mathrm{CF}(\theta) \times \beta_p^{\mathrm{meas}}(\theta)$, can be used to validate and correct LISST measurements with scattering predicted from Mie theory. Values of the correction function varied in the range 1.7-2.2 in this study. Moreover, laboratory measurements were done on natural seawater samples from different marine environments around the Southern California coast. In addition, the degree of linear polarization was also thoroughly investigated in a similar fashion, showing the further potential of LISST-VSF measurements. This work was very recently expanded upon in [25], where relationships between the measured Mueller matrix components and marine particle properties were investigated. The LISST-VSF has also been used in some optical communication studies (e.g. [26,27]), and in Sahoo et al. [28], where measurements were done *in situ* at discrete depths in the Bay of Bengal.

Optics EXPRESS

While earlier studies have used the default relative calibration, Hu et al. [29] offered a significant improvement with the implementation of an absolute calibration of the eyeball detector (see section below for details). This decouples the two detector measurements and enables VSF measurements in very clear waters, which was utilized in a study where the VSF fraction of particles smaller than 0.2 and 0.7 $\mu$m in clear ocean waters was measured, in bench-top mode by filtering water during a research cruise in the North Pacific Ocean [30].

In this work, we similarly present results from both submerged polystyrene and polymethacrylate beads and natural waters using the LISST-200X and LISST-VSF. Our approach to absolute calibration utilize larger beads and has a larger concentration range than most earlier studies, which to a greater extent indicates the validity ranges of the instruments. Polarization measurements with the LISST-VSF, the Mueller matrix components $M_{12}$ and $M_{22}$, have not been included in the study for brevity. The focus of the natural water measurements has been *in situ* data collection using profiling deployment. Fieldwork has been conducted in highly diverse environments, such as the Arctic Ocean and coastal waters of the Svalbard archipelago during the INTAROS-2018 and CAATEX-2019 cruises, and in various coastal waters in southwestern Norway. We evaluate the need for temperature and salinity corrections, compare the validity ranges of the two instruments, and assess the effect of Schlieren on measurements in stratified waters. Finally, we look into extrapolation of forward scattering to estimate the scattering coefficient, which could be another useful application for the LISST-200X in turbid waters.

## 2. Methodology

### 2.1. Laboratory calibration measurements

Spherical beads with microscopic, low-variance diameters, made by polystyrene or polymethacrylate, made it possible to perform absolute calibration or validation of scattering measurements. Knowing the bead size distribution, relative refractive index and concentration, Mie theory can be used to calculate the exact VSF of the plastic beads submerged in pure water. Consequently, measurements from the LISST instruments may be compared with accurate theoretical values. For the relative complex refractive index of polystyrene beads, we used values found in [31]. For polymethacrylate (PMMA) beads, values from [32] were used. Theoretical scattering was calculated using Gaussian particle size distributions with the specified size variations. Each VSF was converted to instrument-specific angular resolutions by finding the mean value within each angular bin, which corresponds to the assumption made by the instrument data processing. For transmission values within the instrument range, the VSF measurements have been corrected for volume concentration errors by re-scaling using the ratio of measured and theoretical attenuation, similar to the method used in [11] and [24],

$$\beta_{\mathrm{corr}}(\theta) = \frac{c_{\mathrm{Mie}}}{c_{\mathrm{meas}}}\beta_{\mathrm{meas}}(\theta). \tag{5}$$

The motivation for doing bench-top measurements using beads are different for each of the studied sensors. The LISST-VSF ring detectors have already been factory-calibrated for VSF measurements, so validation is the primary goal. The LISST-200X has not been directly calibrated for VSF measurements, meaning that absolute calibration is necessary. For the LISST-VSF eyeball detector, the current default data processing uses a relative calibration to calculate the VSF, where the VSF measured from two outer-most ring detectors (angles 12.32° and 14.38°) are extrapolated to the first angle of the eyeball detector (15°). The ratio of the extrapolated value and the uncalibrated eyeball detector value $P_{11}^{\mathrm{uncal}}(15)$ is subsequently used as a scaling factor for calculating the VSF from $P_{11}^{\mathrm{uncal}}(\theta)$. This method is highly sensitive to uncertainties in the ring scattering data.

In addition, bead measurements spanning over a large concentration range allow an assessment of the validity of the VSF measurements; when does the linear relationship between particle

Optics EXPRESS

concentration and VSF, or attenuation, break down? The topic of instrument validity ranges with respect to particle size and concentration is further discussed in section 3.1.1.

#### 2.1.1. Overview of data processing

The VSF is computed from scattering data output of the LISST instruments, digital counts, using factory-provided data processing procedures outlined here. The ring detector data processing has been treated in detail in [3,10]. The raw signal, denoted scat, is digital counts, from which ambient light has been rejected. This is corrected for instrumental artifacts using

$$\text{cscat} = \text{scat}/\tau - \text{zscat}. \tag{6}$$

Here, zscat are background scattering measurements made in pure water to account for intrinsic pure water scattering and optical losses in the instrument. By contrast to zscat and scat, the corrected scattering signal cscat is no longer an integer due to the division on $\tau$. The transmission ratio is $\tau = T/T_0$, where $T$ is the measured transmission (measured laser power $I_{\text{out}}/I_{\text{incident}}$) and $T_0$ is the measured transmission from the background measurement. LISST-200X cscat values are also divided by a concentration calibration factor (for particle size distribution calculations), yielding many orders of magnitude smaller values than LISST-VSF cscat values. This has no impact on VSF measurements. For the LISST-VSF eyeball detector, the transmission must be calculated from the attenuation $c$, $\tau = \exp(-cL)$, as the pathlength $L$ of the detected light beam varies with the eyeball angle.

The ring cscat data is subsequently converted to the VSF using the expression

$$\beta_{i,p}(\theta) = \frac{P_{i,p}}{P_0} \cdot \frac{C_i}{2\pi\phi(\cos\theta_{i+1} - \cos\theta_i)L}, \tag{7}$$

where $P_{i,p}$ is the cscat scattering data on ring $i$ counted from the centre, $P_0$ is the incident light, $\theta_i$ and $\theta_{i+1}$ is the inner and outer radius of each ring detector, and $\phi = 1/6$ denotes that each detector only covers 1/6 of a circle. Furthermore, $C_i$ represents constants for geometrical corrections such as vignetting. In addition, the sensitivity of the detectors needs to have correct values. The eyeball scattering data follow another processing procedure; four components of scattering data have been measured using combinations of source and detector polarizations. Each of these components are first corrected for ambient light by rapidly turning the laser on and off and subtracting the measured ambient light. Then the components are corrected for differences in transmission due to use of a half-wave plate, before the components are corrected for attenuation-loss and laser drift, and the background measurements (matched with the PMT-gain) are subtracted. At around 45°, there is a change in laser power. This is corrected for using a factory-provided calibration factor, and interpolating the data between 44° and 51°. Moreover, a geometric correction is applied for a small misalignment between laser and eyeball viewing plane, as well as a relative gain correction for differences between the laser polarizations (we used the automatic $\alpha$-value). Finally, the components are used to compute the VSF and additional polarization components. The VSF is computed by first taking the average of the four corrected components, yielding $P_{11}^{\text{uncal}}(\theta)$, which is then scaled using the absolute or relative calibration. We refer to [24,25,29] for further details on the eyeball detector.

#### 2.1.2. Experiment procedure

Each laboratory experiment started with filling the factory-provided sample chambers of the instruments with ultrapure water (Milli-Q). In order to minimize uncertainties in the bead concentrations, care was taken to add an accurate amount of water: 18 mL for the LISST-200X and 1620 mL for the LISST-VSF sample chamber. After adding ultrapure water, at least one hour was allowed for bubbles and possible temperature differences to dissipate, before blank

Optics EXPRESS

measurements were made. For the LISST-VSF, the sample chamber mixers always had to be used when measuring, in order to get non-fluctuating transmission values. Solutions of polystyrene or PMMA beads were then added to the sample chamber using pipettes (Eppendorf Research Plus), so that the bead concentration could be known with a high degree of certainty. For each experiment, a cumulative amount of the bead solution was added, yielding a measurement series of increasing bead concentration. For each bead concentration, approximately 100 single measurements were done with both instruments.

#### 2.1.3. LISST-VSF eyeball detector calibration

Polystyrene beads (0.190 $\mu$m (Sigma-Aldrich); 0.508 and 25.1 $\mu$m (Thermo Fischer Scientific)) in different concentrations were used for the absolute calibration of the LISST-VSF eyeball detector. Following [29], the absolute calibration was implemented with the equation

$$\beta^{\text{eyeball}}(\theta) = \kappa(\theta, V_0)\left(\frac{V_0}{V}\right)^{\gamma} P_{11}^{\text{uncal}}(\theta, V). \tag{8}$$

Here, $V$ is the PMT voltage of the respective measurement and $V_0$ is a reference voltage (selected to be 645 mV in both this and the aforementioned study). The term $(V_0/V)^{\gamma}$ is a conversion factor, yielding a linear relationship between $\beta^{\text{eyeball}}(\theta)$ and $P_{11}^{\text{uncal}}(\theta, V)$ irrespective of PMT voltage. The coefficient $\gamma$ depends on dynode material and geometry; the value used in the Hu et al. [29] study, $\gamma = 8.6$, was also in excellent agreement with our data. Finally, $\kappa(\theta, V_0)$ is the calibration coefficient, which can be calculated from bead measurements and theoretical VSF values using linear regression of Eq. (8).

#### 2.1.4. Ring detector calibration

The LISST-VSF ring detector has been evaluated using polystyrene beads (0.508, 2.504 and 25.1 $\mu$m (Thermo Fischer Scientific)) and PMMA beads (4.92 $\mu$m(Sigma-Aldrich)) in different concentrations. We used different angular domains for each type of bead, due to factors described in section 3.1.1. As mentioned above, Koestner et al. [24] introduces a correction function CF, based on bead measurements, which is applied to correct already processed VSF measurements $\beta^{\text{meas}}$. A linear relationship is assumed between the measured and true VSF, so that $\beta^{\text{corr}} = \text{CF} \times \beta^{\text{meas}}$. CF was calculated by finding the median of $\beta^{\text{true}}/\beta^{\text{meas}}$ for each angle, where $\beta^{\text{true}}$ is the theoretical VSF (this is subsequently referred to as method 1). We use a standard least-squares fitting of the measured data to the theoretical values to compute the correction function (method 2),

$$\beta^{\text{true}} = A\beta^{\text{meas}}, \tag{9}$$

and compare with the method stated in [24]. Finally, we also compare with the linear model

$$\beta^{\text{true}} = a\beta^{\text{meas}} + b, \tag{10}$$

to check for possible "zero scattering" offsets in the measured data (method 3).

The LISST-200X was calibrated in a similar way. As the laser power per digital count is not known for the incident laser detector, the default output has the wrong magnitude. Different concentrations of polystyrene beads (2.504 and and 25.1 $\mu$m (Thermo Fischer Scientific)) and PMMA beads (99.0 $\mu$m (Sigma-Aldrich)) were used. The 99 $\mu$m beads were challenging to keep suspended; persistent mixing using a pipette made it possible to measure in the small LISST-200X sample chamber, but not with the LISST-VSF.

### 2.2. Fieldwork

#### 2.2.1. *In situ* measurements

During the field deployments, the LISST instrument measurements were conducted by continuous profiling down to a depth of 50 m, which is the factory-specified maximum operational depth

Optics EXPRESS

of the LISST-VSF. After initial tests, continuous profiling was found to be the prudent choice, as stationary measurements gave highly fluctuating transmission values. This is consistent with bench-top measurements; even when the water is ultrapure, static water is detrimental for transmission measurements. We speculate that this is due to microturbulence along the beam caused by the laser, but mirror-like reflections by large slow-moving particles could also have a contribution. This is not seen for the LISST-200X, but continuous profiling is also used here for consistency. Continuous profiling also puts some constraints on the measurements. The winch system operated with an ascent and descent speed of approximately 0.5 m/s. For the LISST-200X, which has a sample rate of 1 Hz, each sample will then cover 0.5 m. With LISST-VSF, each sample takes 4 seconds. Thus, one sample will cover 2 meters. Moreover, the LISST-VSF acquires data by first doing an eyeball and ring detector measurement with perpendicular polarized incident light, then another with parallel polarized incident light. This means that the Mueller matrix components can only be reliably measured using continuous profiling in a uniform or slowly changing water column. However, the VSF is calculated from a simple average of the different light measurements. To assure high data quality of the LISST-VSF, multiple casts were always made, typically from three in regular waters to seven in very clear waters. The subsequent data processing include depth-binning the measurements and calculating the median VSF. Physical oceanographic quantities have been obtained using the Castaway-CTD or Rockland Scientific VMP-250 vertical profiler.

#### 2.2.2. Locations

*In situ* measurements were conducted during three field campaigns, as well as four different days at the Espegrend Marine Biology Lab in Raunefjorden outside Bergen, Norway (in April 2018, June 2018, June 2019 and November 2019), see Fig. 2 for an overview. During the INTAROS-2018 cruise with the Norwegian coastguard vessel KV Svalbard in the Arctic Ocean north of Svalbard, a total of 9 measurement stations were done. Five stations were conducted around in the region around ice edge as well as in ice leads and under ice floes. The last four stations were made in coastal waters of the Svalbard archipelago, for instance in Rijpfjorden, a fjord on northeastern Svalbard with a large glacier calving into the fjord. More measurements were performed in the central Arctic during the CAATEX-2019 cruise in August-September 2019, also with KV Svalbard. Station 1 of this cruise was conducted at the North Pole, and the proceeding stations were made in the ice-covered ocean south towards Svalbard. Finally, further measurements on glacial meltwater in Norwegian coastal waters were conducted in Gaupnefjorden in June 2019, a fjord arm of Sognefjorden in Western Norway. In total, 25 measurement stations are included in this study, with a significant span in optical characteristics as well as geographical extent.

#### 2.2.3. *In situ* temperature and salinity corrections

In clear waters, the scattering of the water itself may have a significant contribution to the total measured scattering at large angles [30]. Using a blank measurement will remove the scattering at the temperature and salinity of the pure water used. However, the temperature and salinity will almost never be the same *in situ* as the blank, making a temperature and salinity correction necessary. In a previous study, this is addressed by not using a blank for field measurements, but simply subtracting the pure water scattering directly [29]. This assumes no optical losses by the instrument, which may be negligible for new instruments but not after extensive use and time, e.g. increased transmission loss in the optical windows. Thus, we suggest another approach. The measured VSF ($\beta_m$) may be assumed to be the sum of particulate scattering $\beta_p$, pure water scattering $\beta_w$ and optical losses $\beta_L$,

$$\beta_m = \beta_p + \beta_w(T, S) + \beta_L. \tag{11}$$

Optics EXPRESS

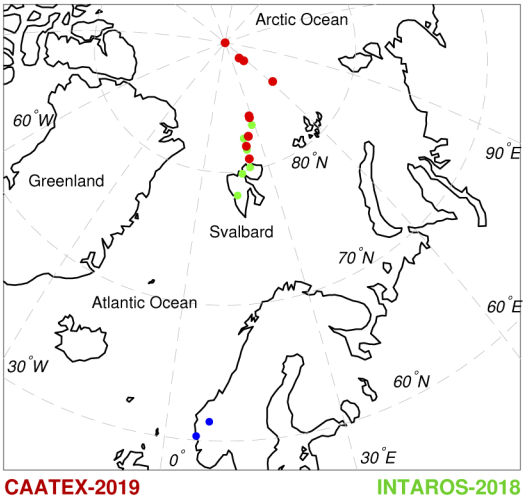


**Fig. 2.** Map showing the locations of the fieldwork conducted in this study. During the INTAROS-2018 cruise (in green) nine stations were conducted. Nine stations were also done during the CAATEX-2019 cruise (in red). Locations of additional fieldwork in Norwegian fjords are shown in blue.

We have not investigated polarization dependencies of the optical loss, but as the scattered light enters the optical window perpendicular (or near-perpendicular) to the window surface, we do not expect major polarized components. For blank measurements, particulate scattering is assumed to be zero, yielding the expression for the measured blank VSF,

$$\beta_{\mathrm{BG}} = \beta_w(T_{\mathrm{BG}}, 0) + \beta_L. \tag{12}$$

Since the optical loss term is the same in both instances, one can solve for the particulate scattering,

$$\beta_p = \beta_m - \beta_{\mathrm{BG}} - \beta_w(T, S) + \beta_w(T_{\mathrm{BG}}, 0). \tag{13}$$

Here, the term $\beta_m - \beta_{\mathrm{BG}}$ is the output of the default data processing. The pure water scattering is calculated as described in [33] and [34]. The temperature and salinity from field work are interpolated from CTD measurements.

## 3. Results and discussion

### *3.1. Laboratory measurements*

#### 3.1.1. Validity ranges for LISST measurements

The validity range of the LISST instruments is limited by the range of the detectors, as well as the assumption that all scattered light is only scattered once (single-scattering condition). The instrumental validity ranges are also evident from the bead calibration measurements. To get stable and consistent measurements for calibration use, the VSF must vary slowly due to possible smearing effects, the oscillations characteristic for beads must be absent or smoothed out. Small beads (for instance 0.190 $\mu$m diameter) fit this requirement well, but the LISST instruments are optimized for natural waters, which have implications for the lower signal limit of the ring detectors. In Fig. 3(a), it can be seen that when cscat-values $<10^{-4}$, LISST-200X VSF measurements only have a weak relationship with theoretical VSF values compared to above this threshold. For reference, cscat values from field measurements are typically in the range $10^{-5}$ to $10^{-2}$. For LISST-VSF, the same is seen for cscat-values $<10^{2}$ in Fig. 3(b) (LISST-VSF

Optics EXPRESS

cscat values are typically between $10^2$ and $10^5$ in field measurements). This pattern is seen for all ring detectors for similar cscat values. Given that the scattering data are related to the VSF through Eq. (7), the minimum VSF values will vary with angle. Field scattering data within these orders of magnitude should be treated with care. Within the low particle concentration limit, the transmission reaches the upper detection limit (which is given as 0.98 for LISST-VSF and 0.995 for LISST-200X). The transmission errors have a relatively low impact on scattering data in clear waters, as seen from Eq. (6).

Within the high particle concentration limit, the transmission lower limit has a large impact. Following Eq. (6), the scattering data are highly sensitive for errors in the transmission measurements when the transmission is low. However, multiple scattering is a more likely limiting factor for VSF measurements in turbid waters. Re-scattered light enters the detectors in addition to the single-scattered light, leading to an overestimation of the VSF. The single-scattering condition is commonly given as $\tau^* << 1$, where $\tau^* = cL(1-g)$ is the scaled optical depth ($L$ is the pathlength, $c$ is attenuation), not to be confused with the transmission ratio $\tau$. The appearance of the asymmetry parameter $g$ shows that for waters with smaller angular differences in the VSF, the single-scattering condition will be violated at lower concentrations than in waters with a dominant forward scattering component. When planning the measurements, we used $\tau^* \leq 0.1$ as a default condition.

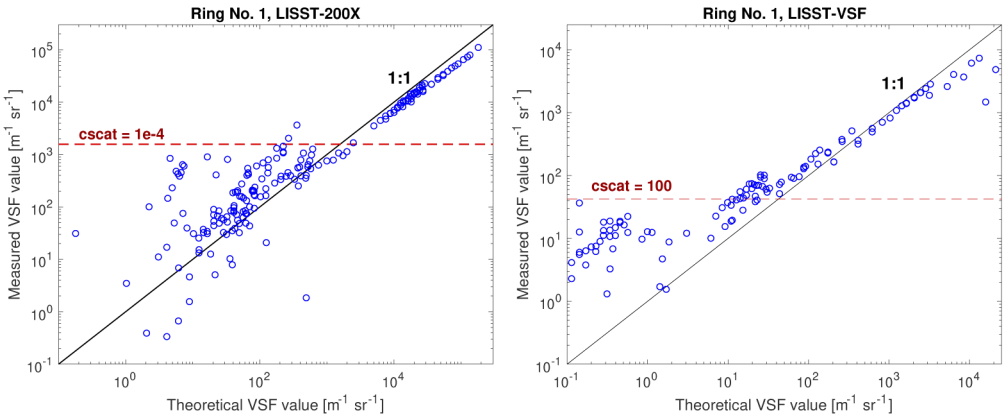


(a) LISST-200X (b) LISST-VSF

**Fig. 3.** The VSF of polystyrene or PMMA beads, measured with the innermost ring detector on both instruments and compared with the theoretical values computed using Mie theory. Under a certain threshold in the scattering data (cscat), there is a loss of linearity between measured and predicted values. Due to the area of the rings, this problem is most prevalent for the innermost rings, and dissipates at larger angles, where the size of the detector is larger.

The expected range of possible bead concentrations due to the some of the aforementioned factors are visualized in Fig. 4. Here, Mie calculations have been applied to polystyrene beads of diameters 0.1-200 $\mu$m, and for the wavelengths of both LISST instruments. There is a scattering maximum for particle diameters approximately twice the wavelength, leading to a minimum of the detectable volume concentration. For smaller particles in the Rayleigh limit, the range of valid volume concentration becomes smaller. Large particles can have much higher volume concentrations without violating the single-scattering condition, and lower concentrations to get strong signals for the ring detector. However, large beads are limited by oscillations for larger angles. Measurements at these angles were excluded in the calibrations. Thus, for calibrating

Optics EXPRESS

LISST instruments at all angles, it is necessary to include measurements with both smaller and larger beads.

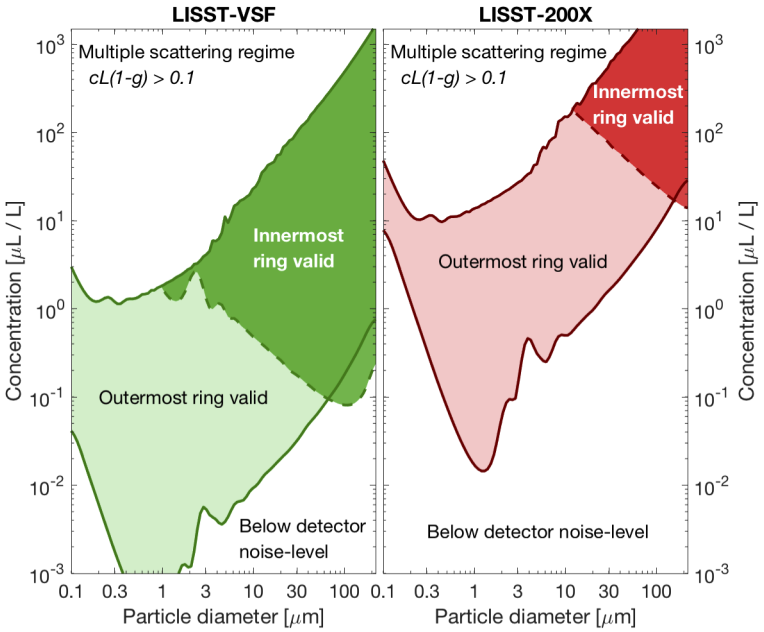


**Fig. 4.** Expected concentration range for valid measurements calculated for mono-dispersed polystyrene beads, varying in size and diameter. Red area shows the valid area for LISST-200X (wavelength 670 nm) and green area for LISST-VSF (wavelength 515 nm). The strongly colored areas indicate the concentration range needed to get valid measurements for the innermost rings, while the weakly colored areas indicate concentrations for valid signal from the outermost rings. The areas are overlapping, except in a small region with low concentrations of large beads. Here, scattering is so forward-peaked that there is a valid signal for the inner ring but not the outer ring. It should be noted that these results do not extend to particle size distributions.

In this study, we have used six bead diameters covering different angular domains. When calibrating the LISST-VSF, 0.190 $\mu$m beads were used for angles above 15°, and 0.508 $\mu$m beads above 5.5°. Furthermore, 2.504 $\mu$m beads were used for angles below 4.7° and 3.92 $\mu$m beads below 2.1° (both with limited signal under $\sim$ 0.3°). Finally, 25.1 $\mu$m beads were used in the angular domains 0.09° – 0.75° and 4.7° – 14.4°. For the LISST-200X, 2.504 $\mu$m beads were used for angles below 10° (with limited signal under 0.1°), and 25.1 $\mu$m beads were used in the angular domains 0.07° – 1° and 3.5° – 13°. In addition, 99 $\mu$m beads were of particular importance to get data for the innermost rings, covering the angular domains 0.04° – 0.2° and 2.5° – 13°.

### 3.1.2. Bead attenuation measurements

The results of the attenuation measurements are shown in Fig. 5(a) and 5(b). The measurements show overall high agreement with the theoretical values when transmission values are higher than 98 %. For lower attenuation values, the measurements become imprecise. Some measurements with the LISST-200X have high variability also for higher attenuation. The 99 $\mu$m beads used were difficult to sufficiently mix for avoiding settling. Other deviations may be explained by uncertainties in the volume concentration. Comparing the two instruments, the results support the notion that LISST-VSF is suited for attenuation measurements in all but extremely clear natural waters ($c$>0.13 m$^{-1}$), while the LISST-200X is more limited ($c$>0.8 m$^{-1}$). The upper

Optics EXPRESS

limit of neither instrument has been reached, the LISST-VSF results show good accuracy up to $\sim 30\ \mathrm{m}^{-1}$, above the specified limit.

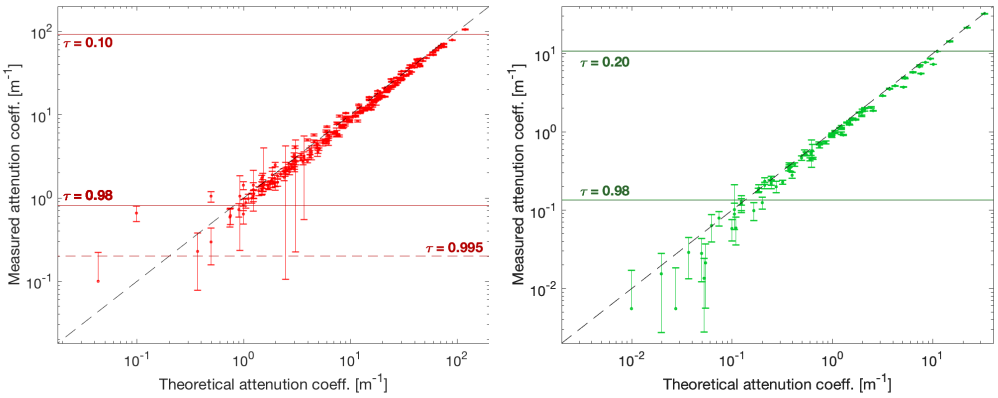


(a) LISST-200X (b) LISST-VSF

**Fig. 5.** Attenuation measurements with the LISST-200X and LISST-VSF using plastic beads; comparison between theoretical values from Mie theory and measured values. Error bars indicate the standard deviations in each measurement, consisting typically of around 100 samples. The factory-specified limits for valid transmittance measurements $\tau = \exp(-cL)$ are also plotted.

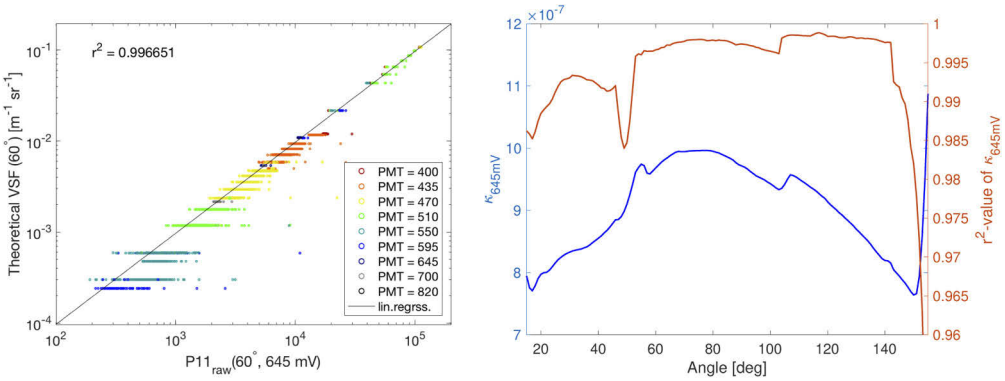


(a) (b)

**Fig. 6.** The absolute correction for the eyeball detector is found by linear regression of $P_{11}^{\mathrm{uncal}}(\theta, 645\ \mathrm{mV})$-values and theoretical VSF-values for each measured angle. In (a), uncalibrated LISST-VSF eyeball detector data $P_{11}^{\mathrm{uncal}}(\theta, 645\ \mathrm{mV})$ (converted to PMT = 645 mV, see Eq. (8)) are compared with corresponding theoretical VSF values for $\theta = 60°$. Different colors differentiate the PMT values. The linear regression yielding the $\kappa$-value is also plotted. In (b), the absolute calibration factor $\kappa$ is plotted over the entire angular domain of the LISST-VSF eyeball detector output (blue line). The coefficient of determination ($r^2$-value) is also shown for each angle.

Optics EXPRESS

### 3.1.3. LISST-VSF eyeball detector calibration

The PMT correction of the LISST-VSF was made with 0.190, 0.508 and 25.1 $\mu$m polystyrene beads over a large concentration range. Similar to the Hu et al. study [29], a strong linear relationship between the $P_{11}^{\text{uncal}}(\theta, 645\text{mV})$ and $\beta^{\text{eyeball}}(\theta)$ can be seen in Fig. 6(a) and 6(b). However, the $\kappa$-value is three orders of magnitude smaller for our instrument (SN = 1667), likely because the aforementioned study normalized the $P_{11}^{\text{uncal}}$ by dividing on incident laser power (which could mitigate effects of laser drift). For low 25.1 $\mu$m bead concentrations, which give the lowest VSF values in Fig. 6(a), there is significant variation in the data, possibly due to a relatively low PMT gain compared to the signal. Lack of rescaling (see Eq. (5)), due to attenuation values outside instrument range, may cause additional uncertainties. It should also be noted that comparing goodness-of-fit across the entire angular domain with statistical quantities ($r^2$ or mean square error) should be treated with care, due to large variations in the dynamical range of the measurements, but manual inspection of the data confirms good agreement.

### 3.1.4. LISST-VSF ring detector validation

Measurements of plastic beads up to 25.1 $\mu$m were used to calculate correction functions for the LISST-VSF ring detector. The results are shown in Fig. 7. Near-unity correction functions and $r^2$-values for all methods would indicate a perfect fit between theory and measurements. Figure 7(a) and 7(b) reveal that the ring detector measurements generally agree well with the expected theoretical values for all three methods used. The linearity of the data is illustrated in Fig. 9(a). The correction function found using the median of the ratio (method 1) deviates from the linear regression functions (method 2 and 3) at some angles. The reason seems to be that it is more influenced by where in the scattering range the majority of the measurements have been made. There are no significant differences between the perpendicular (Fig. 7) and parallel (not shown) polarized incident light, as expected for forward scattering. Measurements from the ring detector at 0.90° were highly erratic and non-physical, also in blank measurements. Results from this ring have thus been consistently treated as invalid and replaced by interpolated values using the two neighbor rings, even though this may introduce a small bias.

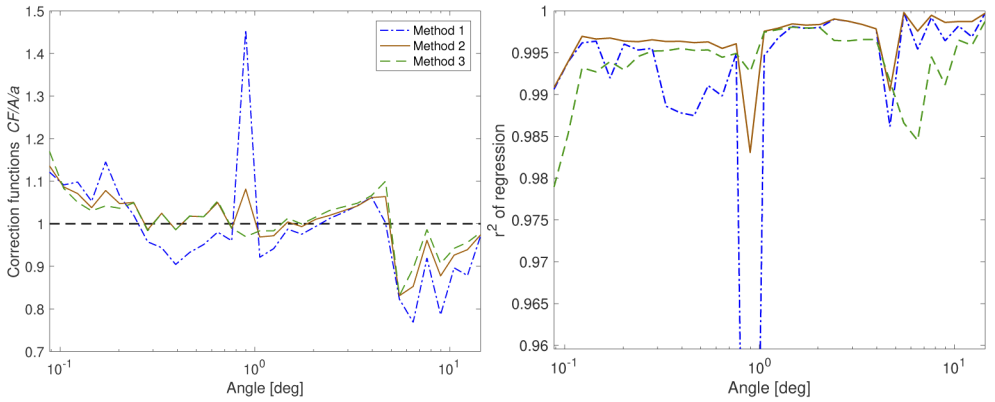


(a) (b)

**Fig. 7.** Correction functions for the LISST-VSF ring detector, for the perpendicular incident beam (first rotation, in the vertical plane of the instrument), is shown in (a). Each method is described in section 2.1.4. The coefficient of determination ($r^2$-value) for each method is shown in (b).

Significantly higher forward scattering than expected from Mie theory were measured for sub-micron beads. The forward scattering varied between measurement series and was observed

Optics EXPRESS

to increase with time. We speculate that this is due to flocculation of small beads, as it has been shown that particle flocculations may appear as larger particles in LISST particle size distribution measurements [35], which is consistent with higher forward scattering. Other studies have used an ultrasonic device to break up the flocs [11,23], which would likely eliminate this error source. Moreover, smaller beads scatters so little in the forward direction that the ring detector scattering data are under the instrument detection level. Data affected by these error sources were discarded. Multiple scattering influences the measurements, which is seen as a non-linear relationship between bead concentration and VSF. This is plotted for 25.1 $\mu$m beads in Fig. 10(a). The single-scattering condition has been used as a guideline ($\tau * <0.1$), but results shown in Fig. 10 indicate that it may not be an adequate condition for calibration purposes, especially for larger beads such as 25 $\mu$m at large angles. Thus, some empirical considerations had to be made for the calibration concentration range. Slade and Boss [11] points out the imaginary refractive index of the bead material as a major error source for VSF measurements of larger beads, but based on Fig. 10 we believe multiple scattering plays a more significant role than expected.

Variations between different particle samples and their dilutions seem to be the largest source of uncertainty. The impact has been mitigated by doing multiple independent measurement series with varying particle diameter and applying the attenuation re-scaling. Nevertheless, it is reasonable to conclude that the deviations may be attributed to the experimental uncertainties, and that the LISST-VSF ring detector is adequately calibrated from the factory.

#### 3.1.5. LISST-200X ring detector calibration

While the VSF is a default output of the factory data processing for the LISST-VSF, the LISST-200X data processing does not yield the VSF by default. However, Sequoia Sci. provided a data processing script enabling non-calibrated VSF measurements as output. Here, the correction functions were used directly for absolute calibration of the measurements. Results shown in Fig. 8 reveal similarities with the LISST-VSF ring detector, including most of the error sources. Figure 9(b) shows an example of robust fit of the data at 0.66°. The correction factors vary between $1.6 \times 10^{11}$ and $3.6 \times 10^{11}$. Method 1 deviates slightly from the two linear regression-methods (method 2 and 3), but follows same the general trend. In Fig. 10(b), one may also for LISST-200X observe a non-linear relationship between attenuation and measured scattering at large angles for 25 $\mu$m beads. In addition, there were some saturation errors in the ring detector data. These measurements had to be manually removed. Following the same considerations as for the LISST-VSF, a constant value, $A = 2.8 \times 10^{11}$, was chosen for all rings.

### 3.2. Field measurements

#### 3.2.1. Assessment of PMT calibration

*In situ* field measurements with particulate scattering covering several orders of magnitude enable robust comparisons between the absolute and relative PMT calibration as well as between the two LISST instruments. A natural point of comparison for the relative and absolute calibration is the VSF at 15°, the start of the eyeball measurement, plotted in Fig. 11. The two methods agree well for mid-range scattering, while discrepancies are apparent in very clear and turbid waters. For clear waters, systematic discrepancies may be seen for PMT-values 435-550. These measurements are from the INTAROS-2018 cruise, where the automatic PMT gain adjustment seemed to insufficiently adjust to very clear waters, yielding noisy eyeball data. After the cruise, the PMT-gain algorithm was updated by the producer, yielding significantly better results for later fieldwork. The absolute calibration was performed after this update. While the PMT gain may be set manually, the automatic gain is typically necessary due to water column variations. Moreover, for the CAATEX-2019 cruise, unreliable values in the outermost ring yielded artificially low eyeball values for the relative calibration, perfectly illustrating the uncertainty of this method. The relative calibration is also visibly affected by random errors in the forward scattering in

Optics EXPRESS

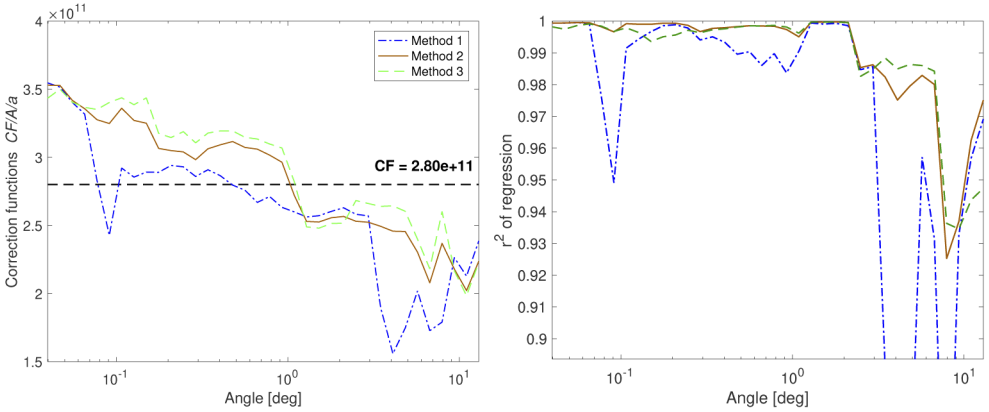


(a) (b)

**Fig. 8.** Correction functions for LISST-200X ring detector is shown in (a). Each method is described in section 2.1.4. The coefficient of determination ($r^2$-value) for each method is shown in (b).

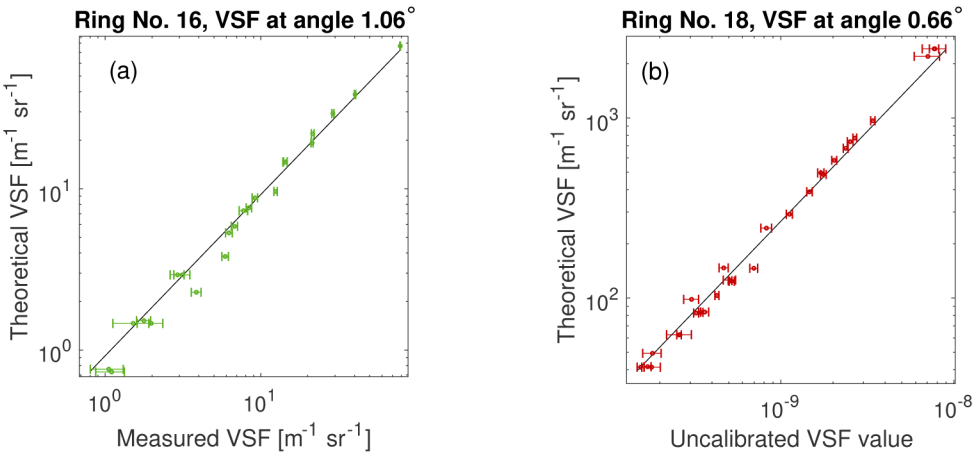


(a) LISST-VSF (b) LISST-200X

**Fig. 9.** Measured VSF from ring 16 of the LISST-VSF ring detector (total ring number is 32), is compared with theoretically predicted VSF values in (a). The standard deviation of the measurements are plotted as error bars. A robust linear fit (method 2) is also plotted as a black line. In (b), uncalibrated VSF values from the LISST-200X are plotted with corresponding theoretical VSF values, along with the robust fit (method 2, showing ring number 18 out of 36).

addition to the systematic errors in clear waters. In turbid waters, a discontinuity is visible in the VSF between the ring and eyeball detector, at 15° when the absolute calibration is used (see Fig. 14). This is due to multiple scattering effects, as the two detectors have different pathlengths at 15°. The eyeball detector may also experience saturation in particularly turbid media.

The scattering coefficient, backscattering coefficient and backscattering fraction for the two calibrations are compared in Fig. 12(a) and 12(b). All are integrated from bin-median VSF, with extrapolation in the backward direction by using a well-established backscattering model [9]. For $b$, the differences are minimal, due to the dominating contribution of forward scattering to

Optics EXPRESS

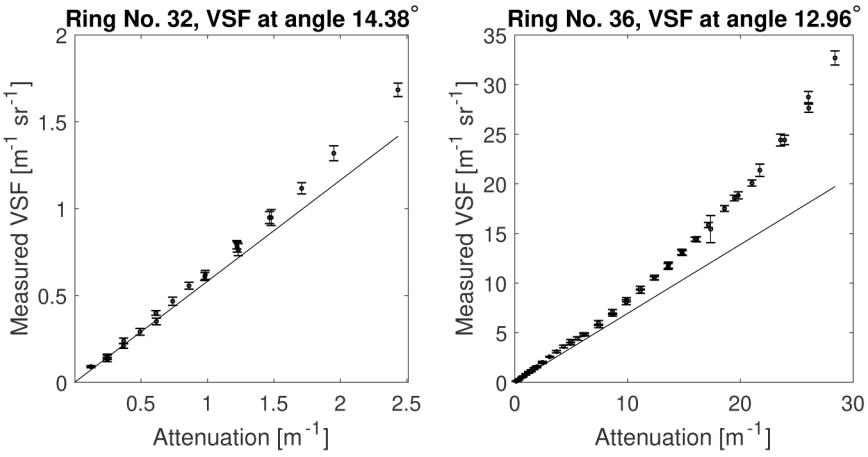


(a) LISST-VSF (b) LISST-200X

**Fig. 10.** VSF measurements with 25.1 $\mu$m beads are plotted as a function of the attenuation, for the outermost ring of LISST-VSF (a) and LISST-200X (b). Theoretically predicted scattering is plotted as a black line. Maximum scaled optical depth for the LISST-VSF results is $cL(1-g) \sim 0.02$, for LISST-200X the maximum value is $cL(1-g) \sim 0.05$. Non-linear behaviour can be seen for a large range of concentrations. In the innermost rings the non-linear behaviour is absent (not plotted).

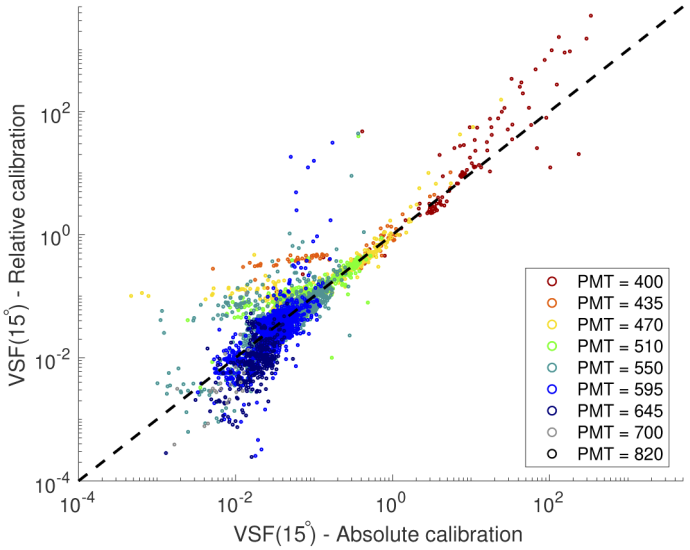


**Fig. 11.** Comparison of LISST-VSF measurements at 15°, using relative (default calibration) and absolute calibration. Each color represents a different PMT value used in the calibration. As the PMT values may change throughout a profile, each measurement is plotted. While most measurements are close to the 1:1 line, there are differences in turbid and very clear waters.

Optics EXPRESS

the scattering coefficient. By contrast, $b_b$ shows more discrepancies, especially the effects of multiple scattering are apparent.

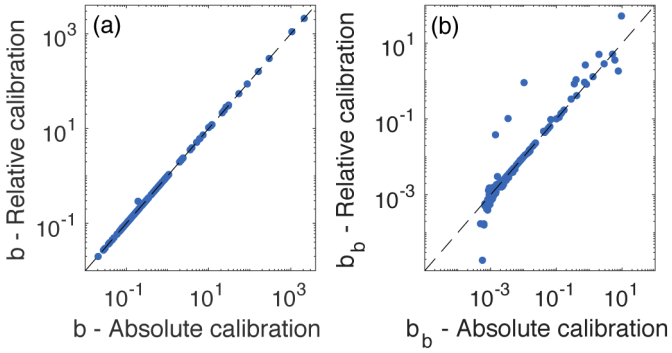


**Fig. 12.** Comparison of the particulate scattering coefficient $b$ (a), the particulate backscattering coefficient $b_b$ (b), when using the relative and absolute calibration.

### 3.2.2. Temperature and salinity corrections

In Fig. 13, absolute calibrated LISST-VSF measurements are plotted with the offset due to pure water scattering, computed from temperature and salinity interpolated from CTD measurements. It is clear that a temperature and salinity correction is important for clear waters, but it gives a negligible contribution at small angles or in turbid waters. LISST-200X has a measurement domain which does not reflect a need for a temperature and salinity correction of the VSF. The importance of auxiliary CTD casts is evident in almost all investigated waters, as changes in both optical and physical quantities are often significant in the upper water column. Natural waters with high salinity and low temperatures have the highest pure water scattering, with the salinity making the strongest contribution. Most physical and empirical models that are used in the computation of pure water scattering, have a validity range down to 0 °C. In polar surface waters, the water temperature can be lower than -1.5 °C. Few studies have investigated optical properties at such temperatures. A theoretical model for volume scattering function by pure seawater was recently extended to subzero temperatures by [36]. For *in situ* measurements, one also need to consider possible offsets in light attenuation and the refractive index [37]. In particular, changes in the latter leads to a different transmittance at the interface between water and optical windows. Estimates show that these effects combined can give an absolute error in the attenuation up to ~0.01 $m^{-1}$ for LISST-VSF, and ~0.05 $m^{-1}$ for LISST-200X. VSF measurements are less affected, with relative errors on the order of $\sim 10^{-3}$. Controlled validation measurements at subzero temperatures and high salinity are needed for more accurate error estimates, instrument-specific corrections, and validation of the theoretical scattering model.

### 3.2.3. Volume scattering function measurements

A selection of particulate VSF measurements in different natural waters is shown in Fig. 14. The values are calculated from the median of all valid data within a given depth-interval (with low variability) at each measurement site. The clearest waters measured in the central Arctic had minimum VSF values of $\sim 10^{-5}$, with considerable noise even after averaging 138 samples. Only slightly higher scattering, seen at the North Pole station, gives a much less noisy signal. On the upper turbidity limit is glacial meltwater. Here, the measured VSF around 90° is more than five orders of magnitude larger than in the clearest measurements. However, the aforementioned discontinuity between the detectors can be seen at 15°, revealing multiple scattering effects and

Optics EXPRESS

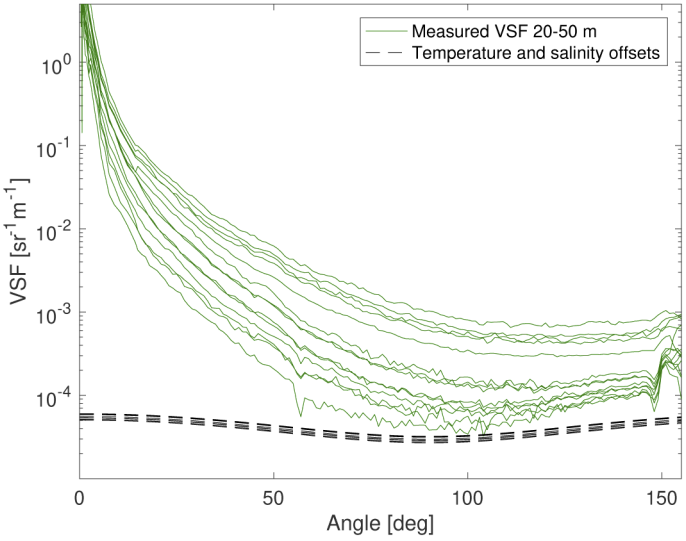


**Fig. 13.** LISST-VSF measurements from a large selection of field measurements (median between 20 and 50 meters), are plotted in green, before correction of temperature and salinity. The temperature and salinity correction offset for each VSF measurement, computed from theoretical pure water scattering [33], is plotted as black dashed lines. Thus, the lines form a band of typical VSF offsets in natural sea water.

suggesting that the detected VSF magnitude may be incorrect. Variations in the phase function are also evident.

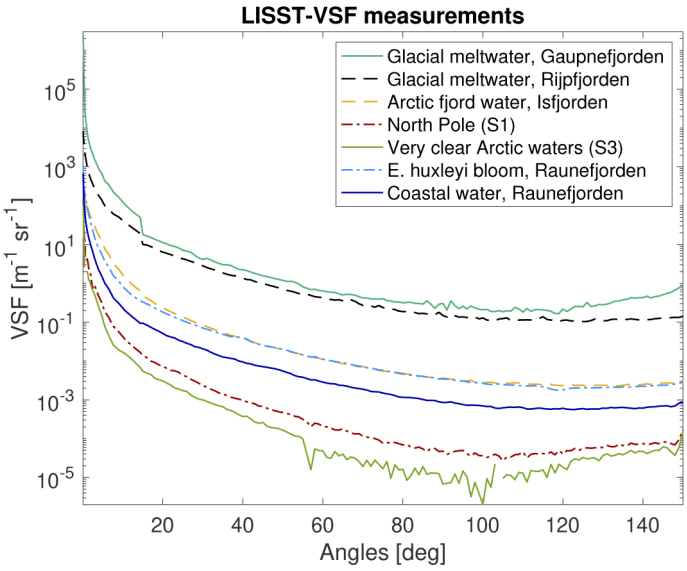


**Fig. 14.** A selection of *in situ* particulate VSF measurements with the LISST-VSF in highly varying natural waters, from the Norwegian coast to the North Pole. The extremities of the instrument validity range can be observed.

In some of the LISST-VSF measurements, a dip can be seen around 120° in the uppermost 10-20 meters. This is most likely because the field-of-view of the eyeball detector moves from

Optics EXPRESS

being directed at the open environment to being directed at the instrument wall at ~120°, leading to an artifact in the ambient light rejection. For angles above 145-150°, elevated VSF values can also be frequently observed (see Fig. 13), both for laboratory and field measurements. The cause is probably instrumental reflections, but backscattering from bubbles could also have an additional contribution.

In Fig. 15, VSF measurements of the LISST-VSF and LISST-200X are compared for three cases. In the lowermost VSF (dashed line), large parts of the LISST-200X falls under the noise level indicated with a solid black line (chosen as cscat = $5 \times 10^{-5}$). The LISST-200X frequently measures scattering under the lower detection level in clear waters, resulting in a unreliable and limited VSF. For the middle case (dashed-dotted line), both instruments perform well. Here, the shape of the VSF agree well, and there is a reasonable increase in scattering from 670 to 515 nm. However, for turbid waters (solid line), the LISST-VSF measures VSF values ~25-500 times higher than corresponding LISST-200X values. These severely elevated measurements are due to multiple scattering. Moreover, the flattening of the LISST-VSF phase function close to zero has been shown to be due to saturated ring detectors. The LISST-200X is with the 2.5 cm pathlength much less influenced by the mentioned effects.

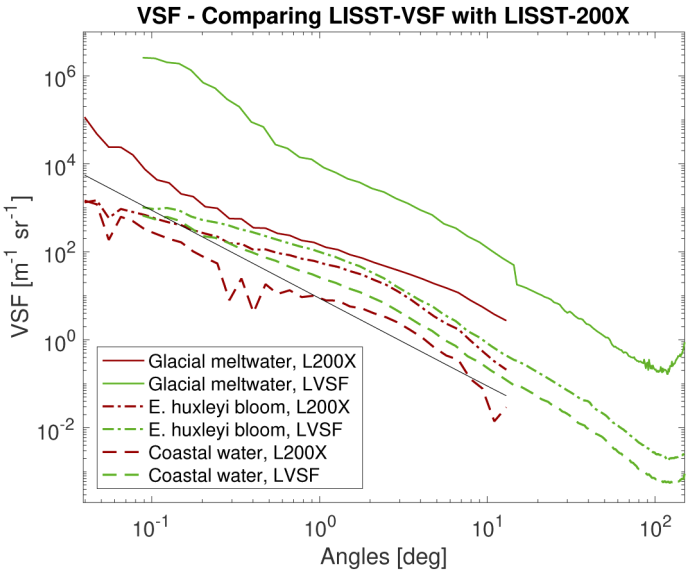


**Fig. 15.** The VSF measured with the LISST-200X and the LISST-VSF are compared for three different cases. Estimated minimum VSF-values that can be measured by the LISST-200X are indicated as a solid red line. Strong systematic errors due to multiple scattering are apparent for the LISST-VSF in turbid glacial meltwater.

### 3.2.4. Estimating scattering coefficient from forward scattering

The dominance of forward scattering on the scattering coefficient ($\beta(\theta<13°)$ contains on average ~80% of $b$) indicates the possibility that LISST-200X measurements can be used to estimate $b$(670nm). LISST-VSF measurements can be used for a robust evaluation, by computing $b$ from both the entire VSF measurement and only the VSF of the LISST-200X angular domain (0.08-13°). The former is computed by using the LISST-VSF measurement up to 145° and the backscattering extrapolation (described in Zhang et al. [9]) up to 180°, which can be assumed to be close to the correct $b$. The latter is computed by curve-fitting the Fournier-Forand VSF to the ring data (up to 13.2°), which is also used for the LISST-200X scattering. An example

Optics EXPRESS

is plotted in Fig. 16. The forward scattering extrapolation tends to systematically overestimate backscattering.

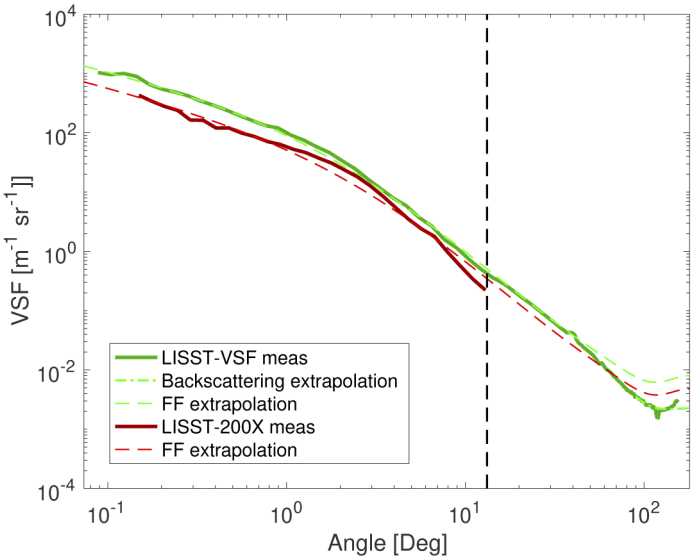


**Fig. 16.** Plot of LISST-VSF and LISST-200X measurements done at the same location and depth (Emiliania Huxleyi bloom, 0.5-10 m), together with extrapolations relevant for estimations of $b$.

In Fig. 17, the two calculated scattering coefficients are compared for a large selection of VSF measurements. Overall, the extrapolated scattering coefficient $b_{FF}$ agrees well with the assumed correct value $b_{corr}$. A tendency to overestimate the scattering for $b$>1 m$^{-1}$ can be seen, but the overestimation of the backscattering has a relatively small impact. Linear regression for $b$<5 m$^{-1}$ gives the correlation shown in Fig. 17, with a 95% confidence interval (assuming a Gaussian distribution) of ±20% on the estimate. Limiting the regression to $b$<1 m$^{-1}$ decreases the confidence interval to ±6%.

Scattering coefficients estimated from LISST-200X measurements (excluding VSF data under the detection limit) are compared with LISST-VSF scattering coefficients measured in the same waters in Fig. 18. Large variations are evident, but the expected trend of generally higher scattering at 515 than 670 nm can be seen. It is also clear that the LISST-200X $b$-estimates are much less affected by multiple scattering than the LISST-VSF values. The related deviations seem to take place above ~2 m$^{-1}$.

### 3.2.5. Schlieren effect

The Schlieren effect is a scattering phenomenon caused by microturbulence and refractive index variations, a prevalent error source for scattering and transmission measurements in stratified natural waters. As Schlieren causes elevated forward scattering, it is primarily affecting the transmissometer and the innermost rings (similar to large particles, leading to errors in PSD calculations). Concurrent profiles with both LISST instruments and CTD instruments make it possible to investigate this effect. This is shown in Fig. 19, where transmission and scattering on the innermost ring of both LISST instruments are plotted with the buoyancy frequency. The buoyancy frequency is a widely used measure on stratification in oceanography, and has in previous studies been linked to Schlieren effects [16–18]. Figure 19(a) shows a clear decrease in LISST-VSF transmission measurements for increased buoyancy frequencies from 0.05 s$^{-1}$. For buoyancy frequencies at 0.15 s$^{-1}$ and higher, many transmission measurements are close to

Optics EXPRESS

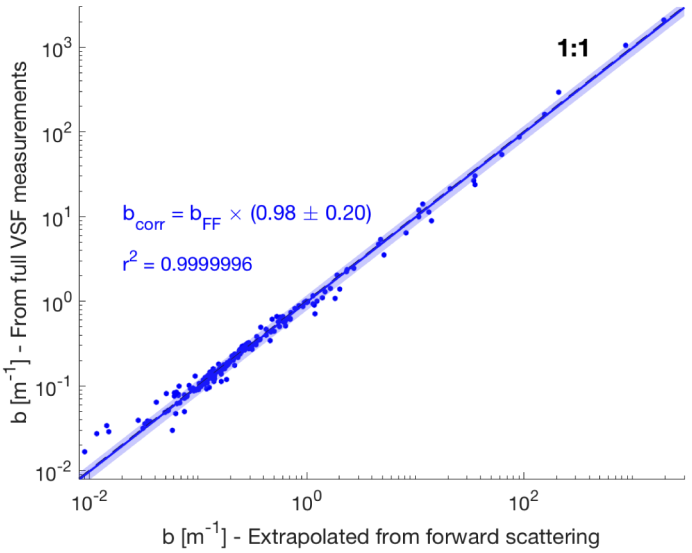


**Fig. 17.** The scattering coefficient estimated from LISST-VSF forward scattering (0.09°-13.2°) compared with the scattering coefficient calculated from the full LISST-VSF measurement (0.09°-145°).

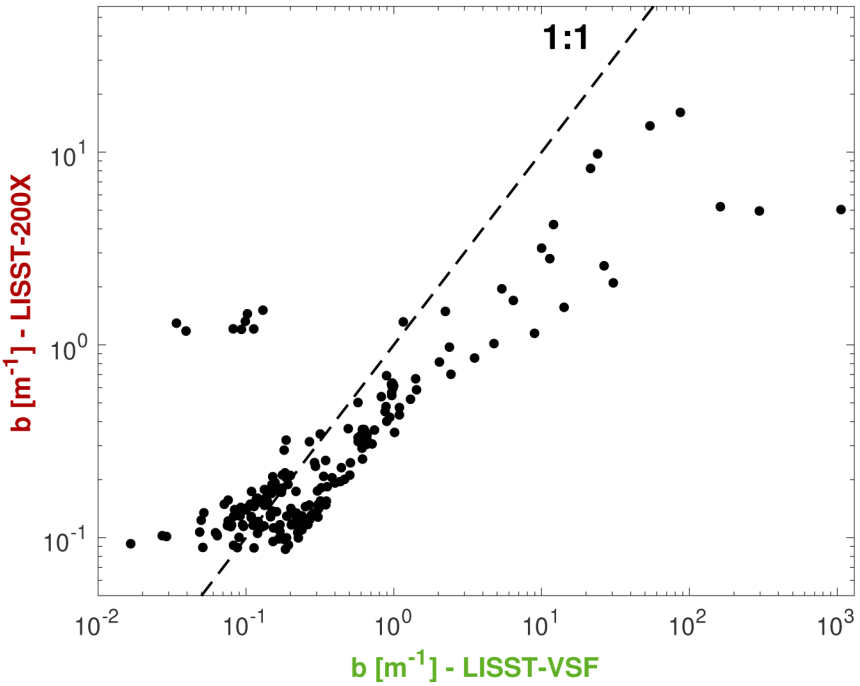


**Fig. 18.** Comparison of scattering coefficients, measured with LISST-VSF and estimated from LISST-200X forward scattering. Large variations can be seen, and LISST-VSF multiple scattering errors seems to occur from ~2 m$^{-1}$.

Optics EXPRESS

being completely extinguished. However, perhaps the most striking feature is the *absence* of data points with both high transmission and buoyancy frequency; there seems to be an upper (lower) limit on the transmission (attenuation), linearly dependent on the buoyancy frequency. A trend is less clear for LISST-200X (Fig. 19(b)), due to the shorter pathlength, but above a buoyancy frequency of ~0.15 $s^{-1}$, large fluctuations in the transmission are prevalent. Increases in the measured forward scattering can also be seen for both instruments (Fig. 19(c) and 19(d)). Ring saturation is also apparent in the LISST-VSF plot. However, it should be emphasized that the scattering measurements are coupled to the transmission through Eq. (6). Thus, suppressed transmission is likely a larger error source for VSF measurements in stratified waters than elevated forward scattering. A final consideration regarding these measurements is that the water density gradient (pycnocline) is associated with particle accumulation and flocculation. Hence, also larger particulate scattering can be expected here, and separating the two phenomena is a considerable challenge.

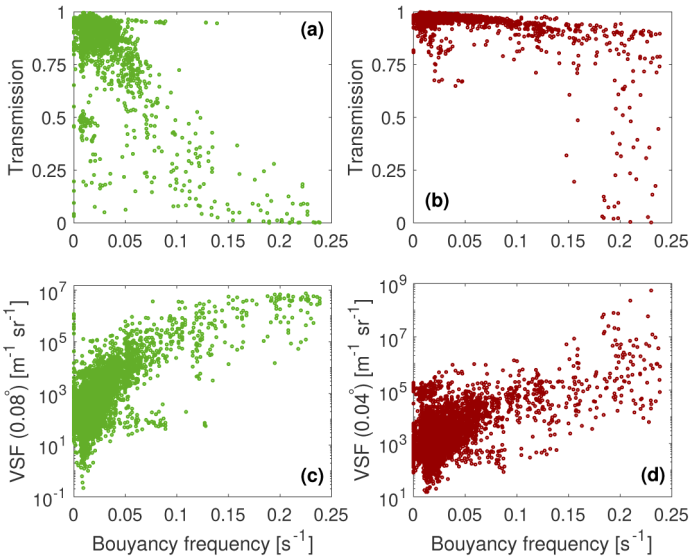


**Fig. 19.** Optical measurements plotted as a function of the buoyancy frequency, visualizing the Schlieren effect on LISST instruments; the transmission of LISST-VSF (a), the transmission of LISST-200X (b), the scattering on the inner-most LISST-VSF ring (c), and the scattering on the inner-most LISST-200X ring (d).

## 4. Conclusion

VSF measurements using the LISST-VSF and LISST-200X have been found to be valid over several orders of magnitude, making them valuable for further *in situ* and laboratory research. Bench-top measurements using monodispersed beads enable absolute calibration of the instrument detectors, but several considerations must be made with regards to instrument noise level, VSF oscillations, possible effects of bead flocculation and multiple scattering. We repeat in large parts procedures performed in earlier studies [11,24,29], but extend the eyeball calibration to a larger range. While the factory calibration of the LISST-VSF ring detector was shown to be satisfactory, the absolute calibration of the eyeball detector has greatly improved the robustness of the VSF measurements, avoiding significant propagation of uncertainties from the two outermost ring detectors to the entire eyeball detector domain. Having two independent detectors with different pathlengths also reveals multiple scattering effects in turbid waters. However, using the absolute

Optics EXPRESS

calibration requires that the PMT gain adjusts itself adequately to the particulate scattering. The lower thresholds of the LISST ring detectors have been given as angular dependent values (cscat $\geq 10^{-4}$ for LISST-200X, cscat $\geq 10^{2}$ for LISST-VSF), but note that these are order of magnitude numbers. The lower limit of the LISST-VSF eyeball detector depends on the PMT gain, and ambient light conditions under some circumstances.

LISST-VSF and LISST-200X have been extensively used in field campaigns, giving valuable knowledge on how to to acquire high-quality data. For LISST-VSF, the water within the sample volume (beam area) must not be static while sampling, either in bench-top mode or during field deployment. The consequence of static water is large fluctuations in transmission and forward scattering. Our speculation is that the laser heats up the water enough to cause microturbulence effects. Hence, continuous descent and ascent is considered best practice during field deployment. For logistical reasons, a profiling speed of approximately 0.5 m/s has primarily been used, but a test with speeds down to 0.1-0.2 m/s have also produced good results. Due to the slow sample rate, we recommend using the lowest practical profiling velocity with the LISST-VSF. Another issue is collecting enough measurements for robust results, which is solved by doing multiple casts and calculating the median VSF, binned with respect to depth. For the LISST-200X, the deployment method is more flexible, but a similar continuous profiling protocol have been used. It has also been shown that temperature and salinity corrections are necessary for LISST-VSF measurements in very clear waters, but are not relevant for LISST-200X measurements.

Comparing the two instruments, their configuration makes them optimized for scattering measurements in different types of natural waters. The LISST-VSF, with its long pathlength, higher laser power and low sample rate, suits clear waters with low scattering, but also coastal waters. In turbid waters with scattering coefficients above approximately 2 $m^{-1}$, multiple scattering errors become significant, but further investigation is needed for details about the effects. LISST-200X is more suited for such waters, with a short pathlength and higher sample rate (which can detect more small-scale variations). However, the scattering and transmission detection levels makes it less suitable for measurements in clear natural waters. The configuration of the innermost rings makes it possible to detect scattering from less than 0.1°, but also makes the measurements vulnerable to errors due to the Schlieren effect. Schlieren has also been shown to significantly affect transmittance measurements, especially for buoyancy frequencies above 0.15 $s^{-1}$, which can have a severe effect on scattering measurements at all angles, as they are corrected by being divided on the transmittance (see Eq. (6)). Thus, care must be taken for measurements in stratified waters.

Even though LISST-200X only measures the VSF up to 13°, it has been shown that by curve fitting the Fournier-Forand phase function to the data, a good estimate of the scattering coefficient at 670 nm can be found. Thus, combined with attenuation measurements, the absorption at 670 nm can be calculated from $a = c - b$. Existing *in situ* spectrophotometers often yield measurements with large scattering-related uncertainties at longer wavelengths [38], especially in turbid waters. Due to its 2.5 cm path-length, the LISST-200X is less susceptible to multiple scattering errors, and may thus yield absorption measurements of higher accuracy than existing instrumentation in such waters. The instrument wavelength (670 nm) lies close to the chlorophyll-a pigment absorption peak at 676 nm. Thus, the instrument may be relevant for use with hyper-spectral *in situ* instrumentation for improved retrieval of primary production estimates in optically complex waters.

## Acknowledgements

We thank the Norwegian Coast Guard, and especially the crew onboard KV Svalbard, for allocation of ship time and excellent field support during the cruise. We also thank the INTAROS and CAATEX project and NERSC for inclusion in the research cruises and support with the cruises. CTD measurements from six stations on the INTAROS cruise were provided by

Optics EXPRESS

Waldemar Walczowski, for which we are grateful. Moreover, Espegrend Marine Biology Lab have been very helpful with the fieldwork in Raunefjorden. Thomas Leeuw at Sequoia Scientific has also been of great help with providing us additional code for the LISST-instruments and answering questions regarding the instruments. Finally, we thank three anonymous reviewers for valuable reviews, which helped us improve upon our manuscript.

## Disclosures

The authors declare no conflicts of interest.

## References

1. D. Blondeau-Patissier, J. F. Gower, A. G. Dekker, S. R. Phinn, and V. E. Brando, "A review of ocean color remote sensing methods and statistical techniques for the detection, mapping and analysis of phytoplankton blooms in coastal and open oceans," Prog. Oceanogr. **123**, 123–144 (2014).
2. P. J. Werdell, L. I. McKinna, E. Boss, S. G. Ackleson, S. E. Craig, W. W. Gregg, Z. Lee, S. Maritorena, C. S. Roesler, C. S. Rousseaux, D. Stramski, J. M. Sullivan, M. S. Twardowski, M. Tzortziou, and X. Zhang, "An overview of approaches and challenges for retrieving marine inherent optical properties from ocean color remote sensing," Prog. Oceanogr. **160**, 186–212 (2018).
3. Y. Agrawal and H. Pottsmith, "Instruments for particle size and settling velocity observations in sediment transport," Mar. Geol. **168**(1-4), 89–114 (2000).
4. X. Zhang, M. Twardowski, and M. Lewis, "Retrieving composition and sizes of oceanic particle subpopulations from the volume scattering function," Appl. Opt. **50**(9), 1240–1259 (2011).
5. N. D. Stockley, R. Röttgers, D. McKee, I. Lefering, J. M. Sullivan, and M. S. Twardowski, "Assessing uncertainties in scattering correction algorithms for reflective tube absorption measurements made with a wet labs ac-9," Opt. Express **25**(24), A1139–A1153 (2017).
6. G. Mie, "Beiträge zur optik trüber medien, speziell kolloidaler metallösungen," Ann. Phys. **330**(3), 377–445 (1908).
7. M. I. Mishchenko, L. D. Travis, and D. W. Mackowski, "T-matrix computations of light scattering by nonspherical particles: a review," J. Quant. Spectrosc. Radiat. Transfer **55**(5), 535–575 (1996).
8. G. R. Fournier and J. L. Forand, "Analytic phase function for ocean water," in *Ocean Optics XII*, vol. 2258 (International Society for Optics and Photonics, 1994), pp. 194–201.
9. X. Zhang, G. R. Fournier, and D. J. Gray, "Interpretation of scattering by oceanic particles around 120 degrees and its implication in ocean color studies," Opt. Express **25**(4), A191–A199 (2017).
10. Y. C. Agrawal, "The optical volume scattering function: Temporal and vertical variability in the water column off the new jersey coast," Limnol. Oceanogr. **50**(6), 1787–1794 (2005).
11. W. H. Slade and E. S. Boss, "Calibrated near-forward volume scattering function obtained from the lisst particle sizer," Opt. Express **14**(8), 3602–3615 (2006).
12. E. Boss, W. H. Slade, M. Behrenfeld, and G. Dall'Olmo, "Acceptance angle effects on the beam attenuation in the ocean," Opt. Express **17**(3), 1535–1550 (2009).
13. Y. Agrawal and O. A. Mikkelsen, "Empirical forward scattering phase functions from 0.08 to 16 deg. for randomly shaped terrigenous 1–21 $\mu$m sediment grains," Opt. Express **17**(11), 8805–8814 (2009).
14. L. Mullen, D. Alley, and B. Cochenour, "Investigation of the effect of scattering agent and scattering albedo on modulated light propagation in water," Appl. Opt. **50**(10), 1396–1404 (2011).
15. X. Zhang, D. J. Gray, Y. Huot, Y. You, and L. Bi, "Comparison of optically derived particle size distributions: scattering over the full angular range versus diffraction at near forward angles," Appl. Opt. **51**(21), 5085–5099 (2012).
16. R. Styles, "Laboratory evaluation of the lisst in a stratified fluid," Mar. Geol. **227**(1-2), 151–162 (2006).
17. O. A. Mikkelsen, T. G. Milligan, P. S. Hill, R. J. Chant, C. F. Jago, S. E. Jones, V. Krivtsov, and G. Mitchelson-Jacob, "The influence of schlieren on in situ optical measurements used for particle characterization," Limnol. Oceanogr.: Methods **6**(3), 133–143 (2008).
18. A. Karageorgis, D. Georgopoulos, W. Gardner, O. Mikkelsen, and D. Velaoras, "How schlieren affects beam transmissometers and lisst-deep: an example from the stratified danube river delta, nw black sea," Medit. Mar. Sci. **16**(2), 366–372 (2015).
19. J. E. Tyler, "Scattering properties of distilled and natural waters 1," Limnol. Oceanogr. **6**(4), 451–456 (1961).
20. T. J. Petzold, Volume scattering functions for selected ocean waters, Tech. rep., Scripps Institution of Oceanography La Jolla Ca Visibility Lab (1972).
21. E. Marken, N. Ssebiyonga, J. K. Lotsberg, J. J. Stamnes, B. Hamre, Ø. Frette, A. S. Kristoffersen, and S. R. Erga, "Measurement and modeling of volume scattering functions for phytoplankton from norwegian coastal waters," J. Mar. Res. **75**(5), 579–603 (2017).
22. W. H. Slade, Y. C. Agrawal, and O. A. Mikkelsen, "Comparison of measured and theoretical scattering and polarization properties of narrow size range irregular sediment particles," in *2013 OCEANS-San Diego*, (IEEE, 2013), pp. 1–6.

Optics EXPRESS


23. T. Harmel, M. Hieronymi, W. Slade, R. Röttgers, F. Roullier, and M. Chami, "Laboratory experiments for inter-comparison of three volume scattering meters to measure angular scattering properties of hydrosols," Opt. Express **24**(2), A234–A256 (2016).
24. D. Koestner, D. Stramski, and R. A. Reynolds, "Measurements of the volume scattering function and the degree of linear polarization of light scattered by contrasting natural assemblages of marine particles," Appl. Sci. **8**(12), 2690 (2018).
25. D. Koestner, D. Stramski, and R. A. Reynolds, "Polarized light scattering measurements as a means to characterize particle size and composition of natural assemblages of marine particles: publisher's note," Appl. Opt. **59**(29), 9233 (2020).
26. B. Cochenour, S. P. O'Connor, and L. J. Mullen, "Suppression of forward-scattered light using high-frequency intensity modulation," Opt. Eng. **53**(5), 051406 (2013).
27. B. Cochenour, K. Dunn, A. Laux, and L. Mullen, "Experimental measurements of the magnitude and phase response of high-frequency modulated light underwater," Appl. Opt. **56**(14), 4019–4024 (2017).
28. R. Sahoo, P. Shanmugam, and S. K. Sahu, "Impact of air–sea interface effects and bubble and particulate scattering on underwater light field distribution: An implication to underwater wireless optical communication system," in *Optical and Wireless Technologies*, (Springer, 2020), pp. 171–178.
29. L. Hu, X. Zhang, Y. Xiong, and M.-X. He, "Calibration of the LISST-VSF to derive the volume scattering functions in clear waters," Opt. Express **27**(16), A1188–A1206 (2019).
30. X. Zhang, L. Hu, Y. Xiong, Y. Huot, and D. Gray, "Experimental estimates of optical backscattering associated with submicron particles in clear oceanic waters," Geophys. Res. Lett. **47**(4), e2020GL087100 (2020).
31. X. Ma, J. Q. Lu, R. S. Brock, K. M. Jacobs, P. Yang, and X.-H. Hu, "Determination of complex refractive index of polystyrene microspheres from 370 to 1610 nm," Phys. Med. Biol. **48**(24), 4165–4172 (2003).
32. S. N. Kasarova, N. G. Sultanova, C. D. Ivanov, and I. D. Nikolov, "Analysis of the dispersion of optical plastic materials," Opt. Mater. **29**(11), 1481–1490 (2007).
33. X. Zhang, L. Hu, and M.-X. He, "Scattering by pure seawater: effect of salinity," Opt. Express **17**(7), 5698–5710 (2009).
34. X. Zhang, D. Stramski, R. A. Reynolds, and E. R. Blocker, "Light scattering by pure water and seawater: the depolarization ratio and its variation with salinity," Appl. Opt. **58**(4), 991–1004 (2019).
35. W. H. Slade, E. Boss, and C. Russo, "Effects of particle aggregation and disaggregation on their inherent optical properties," Opt. Express **19**(9), 7945–7959 (2011).
36. L. Hu, X. Zhang, and M. J. Perry, "Light scattering by pure seawater at subzero temperatures," Deep Sea Res., Part I **162**, 103306 (2020).
37. R. Röttgers, D. McKee, and C. Utschig, "Temperature and salinity correction coefficients for light absorption by water in the visible to infrared spectral region," Opt. Express **22**(21), 25093–25108 (2014).
38. R. Röttgers, D. McKee, and S. B. Woźniak, "Evaluation of scatter corrections for ac-9 absorption measurements in coastal waters," Methods Oceanogr. **7**, 21–39 (2013).